Available online at www.sciencedirect.com
SCIENCE DIRECT®
Journal of Solid State Chemistry 178 (2005) 262–269
JOURNAL OF SOLID STATE CHEMISTRY
www.elsevier.com/locate/jssc

X-ray photoelectron spectroscopy studies of $Yb_{14}MnSb_{11}$ and $Yb_{14}ZnSb_{11}$

Aaron P. Holm[a], Tadashi C. Ozawa[a,1], Susan M. Kauzlarich[a,*], Simon A. Morton[b], G. Dan Waddill[b], James G. Tobin[c]

[a]*Department of Chemistry, University of California, One Shields Avenue, Davis, CA 95616, USA*
[b]*Department of Physics, University of Missouri-Rolla, Rolla, MO 65401-0249, USA*
[c]*Lawrence Livermore National Laboratory, Livermore, CA 94550, USA*

Received 7 January 2004; received in revised form 25 May 2004; accepted 2 July 2004

Abstract

Measurements of core and valence electronic states of single crystals of the rare earth transition metal Zintl phases $Yb_{14}MnSb_{11}$ and $Yb_{14}ZnSb_{11}$ were performed using the X-ray photoelectron spectroscopy station of Beamline 7 at the Advanced Light Source. Sample surfaces of $Yb_{14}MnSb_{11}$ and $Yb_{14}ZnSb_{11}$ were measured as received, after Ar^+ ion bombardment, and after cleaving in situ. The single crystal structure of $Yb_{14}ZnSb_{11}$ is also reported. Both compounds are air-sensitive and show Yb^{3+} due to surface oxidation. In the case of $Yb_{14}MnSb_{11}$, there is no evidence for Yb^{3+} that would be intrinsic to the sample, consistent with previously reported X-ray magnetic circular dichroism studies. Detailed analyses of the $Yb_{14}ZnSb_{11}$ surfaces reveal a significant contribution of both Yb^{3+} and Yb^{2+} 4*f* states in the valence band region. This result is predicted for the Zn analog by Zintl counting rules and support the mixed valency of Yb for $Yb_{14}ZnSb_{11}$. Further detailed analysis of the core and valence band structure of both $Yb_{14}MnSb_{11}$ and $Yb_{14}ZnSb_{11}$ is presented.
© 2004 Elsevier Inc. All rights reserved.

Keywords: XPS; Intermetallic; Zintl phase; Half-metallic; Yb mixed valency; Single crystal

1. Introduction

The family of transition metal compounds with the $Ca_{14}AlSb_{11}$ structure type [1] has shown a wide variety of unique electronic and magnetic properties [2,3]. In particular, the series $A_{14}MnPn_{11}$ show properties ranging from paramagnetic insulators to ferromagnetic metals, depending on the identity of *A* (alkaline earth or rare earth atom) and Pn (pnicogen atom). This class of compounds consists of an isolated magnetic cluster that can magnetically couple over large interionic distances (~1 nm). The magnetic exchange interaction has been attributed to a Ruderman–Kittel–Kasuya–Yosida (RKKY) interaction between localized moments via conduction electrons [3]. This structure type ($A_{14}MPn_{11}$) can be prepared with most 2+ cations such as $A = Ca$, Sr, Ba, Eu, and Yb, with $M = Mn$, Al, Ga, In, Nb, and Zn, and with Pn = P, As, Sb, and Bi [1–8]. One formula unit is composed of 14 A^{2+} cations, one MPn_4^{9-} tetrahedron, one Pn_3^{7-} unit, and four Pn^{3-} isolated anions. The structure has been interpreted according to the Zintl concept, which invokes charge balance between (usually) closed shell structural units such as complexes or extended covalent structures and ions. In this simple model, the Mn is 3+, similar to group 13 metals that also crystallize in this structure type. Both structure and

*Corresponding author. Fax: +1-530-752-4756.
E-mail addresses: jssc@chem.ucdavis.edu, smkauzlarich@ucdavis.edu (S.M. Kauzlarich).
[1]Current address: Department of Electrical Engineering and Electronics, College of Science and Engineering, Aoyama Gakuin University, 5-10-1 Fuchinobe, Sagamihara, Kanagawa 229-8558, Japan.

0022-4596/$ - see front matter © 2004 Elsevier Inc. All rights reserved.
doi:10.1016/j.jssc.2004.07.009

magnetism measurements have been used to support this assignment [3].

A recent report of X-ray magnetic circular dichroism (XMCD) measurements of the compound $Yb_{14}MnSb_{11}$ has produced new information on the source of the magnetic moment in this system, and has increased our understanding of the magnetic interactions in this structure type [9]. The element specific measurements reveal a large dichroism in the L_{23} absorption edge of Mn that is most consistent with Mn in a 2+ (d^5) configuration. There is no dichroism for the Yb, consistent with the presence of Yb^{2+}. In addition to the large Mn dichroism, a small dichroism is observed in the M_{45} absorption edge of Sb. This absorption signal is antialigned to the Mn absorption, and indicates a small magnetic moment lies on Sb that is antiparallel to the Mn moment. These results seem to be inconsistent with the value of $\sim 4\,\mu_B$/formula unit previously reported from bulk magnetization measurements of the compounds that make up the $A_{14}MnPn_{11}$ structure type [3], but a recent theoretical study of the bonding, moment formation and magnetic interactions of the related $Ca_{14}MnBi_{11}$ and $Ba_{14}MnBi_{11}$ systems suggests a new model to account for the discrepancy between electron counting and the experimental data [10]. This study indicates that these phases are nearly half-metallic, and that Mn is present in this structure as Mn^{2+}. It also predicts the presence of a polarized hole localized on the $MnPn_4$ tetrahedron lying parallel to the Mn moment, and resulting in a net $MnPn_4$ moment that is considerably reduced from the ionic Mn^{2+} value. The experimental results are consistent with this theoretical model [9,10].

Another report of thermodynamic, transport, and X-ray diffraction measurements of the related Zintl phase, $Yb_{14}ZnSb_{11}$, has also reported interesting new information related to the Yb analogs of this structure type [7]. This study compares data collected on the Mn, Al, and Zn analogs of this series. The unit cell volume reported from single crystal X-ray diffraction measurements of each of these compounds shows a steady change in volume, with the Zn analog having the smallest unit cell volume. The magnetic susceptibility data are reported for $Yb_{14}ZnSb_{11}$, and show complex magnetic behavior with an effective moment of $3.8 \pm 0.1\,\mu_B$/formula unit, and an average Weiss temperature of -273 ± 10 K. The electrical resistivity data reported for $Yb_{14}ZnSb_{11}$ demonstrate similar behavior to that for $Yb_{14}MnSb_{11}$, but more metallic behavior is demonstrated by the Zn analog in addition to a much broader drop in resistivity at ~85 K in comparison to the sharp drop at 52 K by the Mn analog. The data reported for the Zn analog is explained in terms of an intermediate valence scenario for Yb. The combination of a metallic covalency and a contraction in the unit cell volume both support the presence of an intermediate valence, but they are not conclusive evidence. A comparative study of these Zintl compounds by X-ray photoelectron spectroscopy (XPS) sheds new light on the question of whether an intermediate valence in Yb is present in the Zn analog, and is responsible for the bulk properties reported.

In this paper, we present XPS characterization of the core and valence electronic states of $Yb_{14}MSb_{11}$ (M = Mn, Zn), and in addition, the crystal structure is presented for $Yb_{14}ZnSb_{11}$.

2. Experimental

Single crystal samples of both $Yb_{14}MnSb_{11}$ and $Yb_{14}ZnSb_{11}$ were grown by a high temperature molten metal flux synthesis as described elsewhere [6-7,11]. Single crystal X-ray diffraction data for $Yb_{14}ZnSb_{11}$ were acquired using a SMART 1000 Bruker AXS CCD diffractometer equipped with a CRYO COOLER low temperature apparatus (CRYO INDUSTRIES of America, Inc.). A dark gray crystal (1.5 mm × 1.4 mm × 1.6 mm) of $Yb_{14}ZnSb_{11}$ was cut into a smaller piece (0.03 mm × 0.178 mm × 0.142 mm), and it was mounted in the cold nitrogen gas stream (90 K) of the diffractometer. X-rays were generated at 50 kV and 40 mA using a Mo target and graphite monochromator. A total of 27,196 reflections were collected for the full sphere using a 0.3° ω-scan with a 30 s exposure. Previously published crystallographic data of the Mn analog, $Yb_{14}MnSb_{11}$ [12], were used as a starting model for the refinement. This structure was refined utilizing the SHELXTL-97 software package [13] using 2493 unique reflections and 63 parameters.

Selected samples for the XPS measurements of both $Yb_{14}MnSb_{11}$ and $Yb_{14}ZnSb_{11}$ were characterized by comparing lattice parameters determined by single crystal X-ray diffraction to previously published results (Refs. [7,12]), and also by magnetic susceptibility measurements. XPS measurements were performed in the UltraESCA endstation of Beamline 7.0.1. Samples were mounted on Mo pucks in air, and introduced to the preparation chamber (base pressure 2×10^{-10} Torr). Initial attempts to clean the sample surfaces by Ar^+ sputtering over varying time periods (2–180 min) provided significant improvement from the "as-received" samples, but the best results for sample surface preparation were obtained by cleaving the crystal samples in the preparation chamber using a single blade cleaving tool, and then transferring them to the analysis chamber (1×10^{-10} Torr). A comparison of scans of the Sb 3d/O 1s region (520–540 eV) of the "as-received" samples and those prepared under varying conditions are presented in Fig. 1. No appreciable oxide contamination is present after cleaving of the crystal, but a slight contamination is observed when scanned at the O 1s energy, $h\nu = 900$ eV. In addition, the oxygen peak

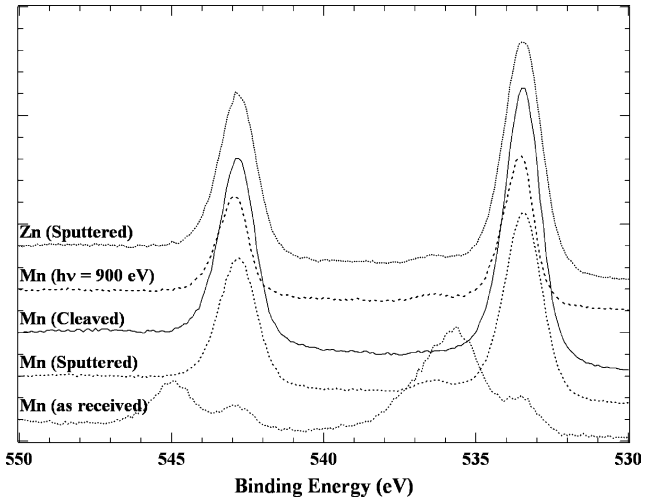

Fig. 1. Comparison of scans of the Sb 3*d*/O 1*s* region (520–540 eV) of the "as-received", Ar^+ sputtered, and cleaved sample surfaces. All scans were measured at $h\nu = 1250$ eV except for the $Yb_{14}MnSb_{11}$ scan measured at $h\nu = 900$ eV.

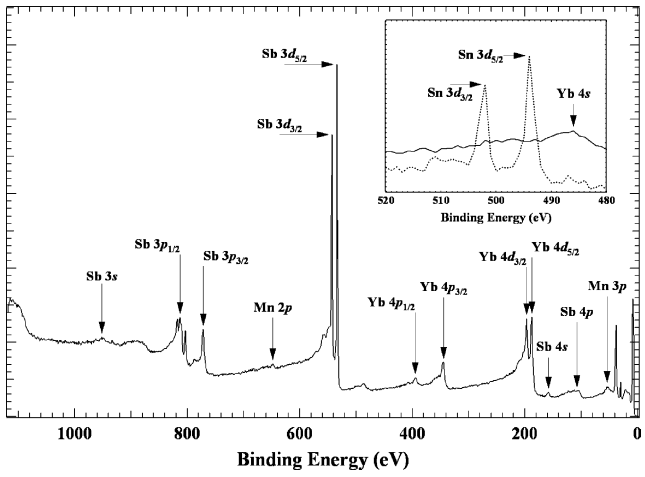

Fig. 2. Wide survey photoemission spectrum of $Yb_{14}MnSb_{11}$ measured at $h\nu = 1250$ eV. The inset presents scans of the "as-received" (dashed line) and cleaved (solid line) crystals of $Yb_{14}MnSb_{11}$ in the Sn 3*d* region (480–520 eV).

grows over time indicating that surface oxidation is extremely rapid even under these low oxygen conditions. Further discussion of this point is given in Section 3. In addition, a check for Sn contamination was performed due to the growth conditions of the samples being in a Sn flux. The inset of Fig. 2 presents scans of the "as-received" (dashed line) and cleaved (solid line) samples in the Sn 3*d* region (480–520 eV). The scan of the "as-received" sample indicates slight Sn contamination due to the presence of the Sn $3d_{5/2}$ and $3d_{3/2}$ core level peaks, but upon cleaving, all indications of Sn are removed with no contribution from the Sn 3*d* states. Photoemission spectra were collected at $T = 93$ K upon cleaved crystals and various photon energies ($h\nu$) between 80 and 200 eV for the valence band scans, and 600 and 1250 eV for the wide surveys and core state surveys. The binding energy of the photoemission structures was calibrated by the Fermi edge of a gold foil mounted next to the samples on the Mo pucks and Ar^+ sputtered immediately prior to cleaving.

3. Results and discussion

The refined crystal structure data for $Yb_{14}ZnSb_{11}$ are summarized in Tables 1–3. $Yb_{14}ZnSb_{11}$ crystallizes in the tetragonal space group $I4_1/acd$ ($Z = 8$). $Yb_{14}ZnSb_{11}$ is isostructural to the Mn analog, $Yb_{14}MnSb_{11}$, which consists of: $14Yb^{2+} + [MnSb_4]^{9-}$ (tetrahedron) + $[Sb_3]^{7-}$ (linear chain) + $4[Sb]^{3-}$ [6,12]. The lattice parameters for $Yb_{14}ZnSb_{11}$ are $a = b = 16.562(3)$ Å and $c = 21.859(2)$ Å at 90 K. The lattice parameters a and b are larger in the Zn analog than in the Mn analog (16.591(1) Å), whereas the lattice parameter c is smaller in the Zn analog than in the Mn analog (21.919(3) Å). The refinement of the site occupancy factor indicated the full occupancies (within the range of their standard deviations) in all sites except a very slight deficiency in the Zn site. Thus, the final refinement was performed with the fixed and full occupancies in all Yb and Sb sites and variable Zn occupancy setting. This refinement shows the Zn occupancy of 0.976(11). The nearest Zn···Zn distance is 9.9216(13) Å, slightly smaller than the Mn···Mn distance (9.9420(6) Å) in the Mn analog.

Fig. 2 shows the wide survey photoemission spectrum of $Yb_{14}MnSb_{11}$ measured at $h\nu = 1250$ eV. The core level states for Yb, Mn, and Sb are present and well resolved near the corresponding positions for the

Table 1
Data collection parameters and crystallographic data for $Yb_{14}ZnSb_{11}$

Empirical formula	$Yb_{14}ZnSb_{11}$
Crystal size (mm^3)	$0.03 \times 0.178 \times 0.142$
Space group	$I4_1/acd$
Z	8
Temperature (K)	90
Unit cell dimensions (Å)	$a = 16.562(3)$
	$c = 21.859(2)$
Volume ($Å^3$)	5995.9(16)
Formula weight (g/mol)	3827.18
Reflections collected	27196
Unique reflections	2493
Parameters refined	63
Max. and min. transmissions	0.4134 and 0.0330
μ Mo$K\alpha$ (mm^{-1})	26.83
$R_1[I > 2\sigma(I)]$ [a]	0.0438
wR_2 [b]	0.0841

[a] $R_1 = ||F_0| - |F_c||/\Sigma|F_0|$.
[b] $wR_2 = \Sigma[w(F_0^2 - F_c^2)^2]/\Sigma[w(F_0^2)^2]^{1/2}$.

Table 2
Atomic coordinates, site occupancy, and anisotropic displacement parameters (Å^2)

Site	x	y	z	SOF	U_{eq} [a]
Sb(1)	0.13556(4)	0.38556(4)	0.125	1	0.00403(18)
Sb(2)	0.00440(4)	0.10934(4)	0.81037(3)	1	0.00457(15)
Sb(3)	0.86954(4)	0.97338(4)	0.95268(3)	1	0.00497(15)
Sb(4)	0.0000	0.2500	0.1250	1	0.0048(3)
Yb(1)	−0.04223(3)	−0.07373(3)	0.828290(17)	1	0.00458(11)
Yb(2)	−0.02164(3)	0.12496(3)	0.001630(18)	1	0.00601(11)
Yb(3)	0.35534(4)	0.0000	0.2500	1	0.00425(13)
Yb(4)	0.17998(3)	0.40937(3)	0.842610(18)	1	0.00601(11)
Zn(1)	0.0000	0.2500	0.8750	0.976(11)	0.0053(7)

[a] U_{eq} is defined as one-third of the trace of the orthogonalized U_{ij} tensor.

Table 3
Selected inter-atomic distances (Å) and angles (deg)

Sb(1)–Sb(4)	3.1750(11)
Sb(1)–Yb(1) × 2	3.1750(11)
Sb(1)–Yb(2) × 2	3.2958(7)
Sb(1)–Yb(3)	3.3288(5)
Sb(1)–Yb(4)	3.1607(10)
Sb(2)–Zn × 4	2.7255(8)
Sb(2)–Yb(1)	3.1531(10)
Sb(2)–Yb(1′)	3.1830(8)
Sb(2)–Yb(2)	3.6957(10)
Sb(2)–Yb(2′)	3.1169(9)
Sb(2)–Yb(3)	3.2276(10)
Sb(2)–Yb(4)	3.1492(10)
Sb(2)–Yb(4′)	3.3925(9)
Sb(3)–Yb(1)	3.1680(10)
Sb(3)–Yb(1′)	3.1840(8)
Sb(3)–Yb(2)	3.1617(10)
Sb(3)–Yb(2′)	3.2704(10)
Sb(3)–Yb(3)	3.1250(10)
Sb(3)–Yb(4)	3.1989(8)
Sb(3)–Yb(4′)	3.1782(8)
Sb(3)–Yb(4″)	3.6896(11)
Sb(4)–Yb(1) × 4	3.1709(7)
Sb(4)–Yb(2) × 4	3.4190(5)
Sb(2)-Zn–Sb(2′)	105.584(14)
Sb(2)–Zn–Sb(2″)	117.56(3)
Zn⋯Zn	9.9216(13)

elements in their natural forms [14]. The Sb 3*s*, $3p_{1/2}$, $3p_{3/2}$, $3d_{3/2}$, $3d_{5/2}$, and 4*s* core levels are observed at binding energies of 952.0, 813.0, 772.0, 543.0, 534.0, and 158.0 eV, respectively, and are within ~1 eV of the tabulated peak positions. The peak separations of the spin–orbit split partners correspond to the tabulated differences to within ~1 eV difference. The states of Sb $4p_{1/2}$ and $4p_{3/2}$ core levels are not resolved, but peak intensity at 108.0 eV is present corresponding to Sb 4*p*. The Yb 4*s*, $4p_{1/2}$, $4p_{3/2}$, $4d_{3/2}$, and $4d_{5/2}$ core levels are present at binding energies of 486.0, 395.0, 345.0, 197.0, and 188.0 eV, respectively. The Yb peak positions are all within ~7 eV of the tabulated peak positions, and spin–orbit split peak differences are all within 1 eV of tabulated differences.

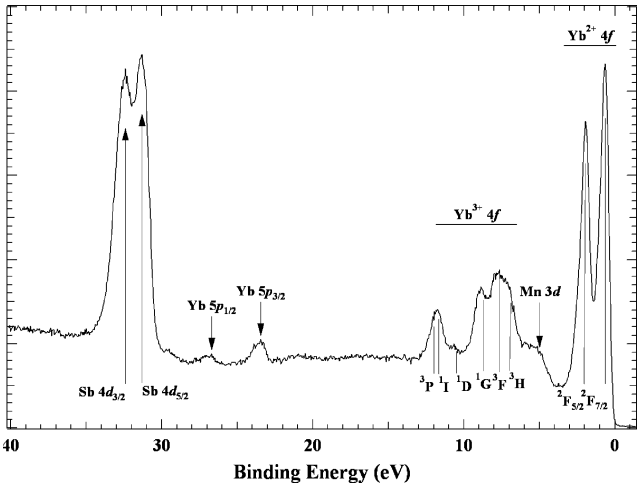

Fig. 3. Valence band scan of $Yb_{14}MnSb_{11}$ measured at $h\nu = 120$ eV.

Fig. 3 shows the valence band scan of $Yb_{14}MnSb_{11}$ measured at $h\nu = 120$ eV. The general spectral shape of the complete region studied remained consistent over the complete photon energy range studied ($h\nu = 80-200$ eV). The core level, spin–orbit split Sb $4d_{3/2}$ and $4d_{5/2}$ states, and Yb $5p_{1/2}$ and $5p_{3/2}$ states can be seen at 32.40, 31.30, 26.70, and 23.45 eV, respectively. A distinct and sharp doublet structure with a width of ~3 eV dominates the Fermi edge region due mainly to the final state multiplets, $^2F_{5/2}$ and $^2F_{7/2}$, from the photoionization of a 4*f* electron from the filled Yb^{2+} shell. A broad multiplet structure is also visible between 4 and 13 eV that has been identified as the 4*d*–4*f* resonance emission from Yb^{3+}. The 4f intensities can be enhanced by using a photon energy, corresponding to the 4*d* binding energy (182.7 eV). Under these conditions, a photoemission channel can contribute to the 4*f* intensities, via a 4*d*–4*f* transition followed by an Auger-like decay process to the +1 final state. This allows for confirmation of the peak assignments. The enhanced emission from oxidized Yb^{3+} was observed from spectra taken at 182.7 eV by comparing to a series of spectra

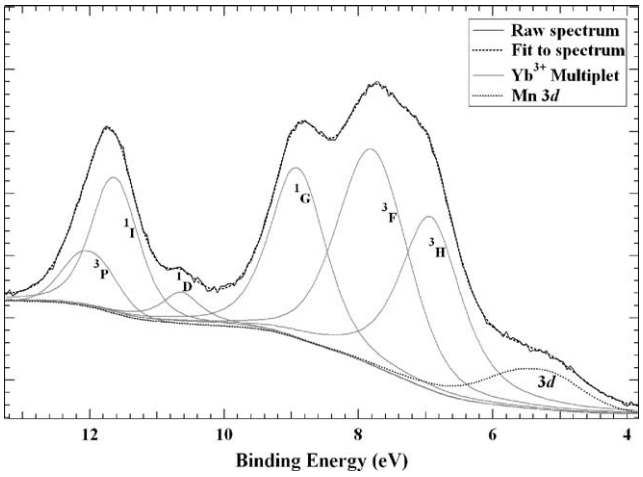

Fig. 4. Gaussian function fit to the Yb^{3+} 4*f* region of $Yb_{14}MnSb_{11}$ measured at $h\nu = 120$ eV using the energy separations observed for the final state multiplets of oxidized Yb in the $4f^{13}$ configuration. The background was fit using a Shirley background, and the peaks were fit using seven Gaussian peaks. The Mn assignment is supported by the spectra shown in Fig. 5.

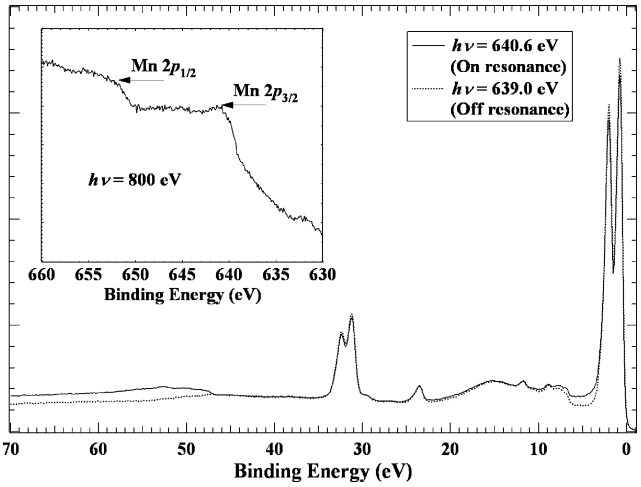

Fig. 5. "On resonance" and "Off resonance" scans from 0 to 70 eV binding energy with an inset showing the Mn $2p_{1/2}$ and $2p_{3/2}$ peaks used to identify the photon energy for the resonance scans of $Yb_{14}MnSb_{11}$.

(taken at 200, 180, 160, 140, 120, 100, and 80 eV) allowed for unambiguous assignment. Fig. 4 shows a fit to the Yb region using the energy separations observed for the final state multiplets of oxidized Yb in the $4f^{13}$ configuration [15–17]. The presence of Yb^{3+} was initially thought to indicate mixed valency of Yb, but further detailed study of the Sb 3*d*/O 1*s* region indicates that a small amount of residual oxide contamination remains. The spectrum taken at $h\nu = 900$ eV in Fig. 1 was measured in order to take advantage of the enhanced ionization cross section for O 1*s* at this photon energy, and indicates a small shoulder, nearly coincident with the Sb $3d_{5/2}$, present at 536.5 eV corresponding to residual surface oxide contamination. It was also noted that these peaks grow over time, supporting the hypothesis that the oxide, the Yb^{3+} are closely associated with a surface oxidation process. In addition, XMCD results show no evidence for Yb^{3+} in the $Yb_{14}MnSb_{11}$ [9].

The identification of Mn core states is much more difficult than the Yb or Sb states due to Mn occupying less than 4% of the total structure. The low concentration of Mn results in the peak intensities being quite low, and the spin–orbit split states not being well resolved. Despite the low concentration of Mn, the 2*p* core level can be seen in the wide survey at ~648.0 eV, but in order to accurately identify the Mn core and valence band states, a resonant photoemission experiment was performed. With the resonant photoemission experiment (640.3 eV for Mn), an enhancement of the direct photoemission process occurs due to a second indirect channel opening up as the absorption threshold of a core level is crossed [18]. For this experiment, the indirect transition occurs by initial excitation of a 2*p* electron to an unoccupied 3*d* level forming a bound intermediate state ($2p^63d^5 \rightarrow 2p^53d^6$), followed by auto-ionization decay to a final state ($2p^53d^6 \rightarrow 2p^53d^5 + e^-$) identical to the final state of the direct photoemission process for the ejected electron. Fig. 5 shows the "On resonance" and "Off resonance" scans from 0 to 70 eV binding energy with an inset showing the Mn $2p_{1/2}$ and $2p_{3/2}$ peaks used to identify the photon energy for the resonance scans. The "On resonance" scan was measured with $h\nu = 640.3$ eV corresponding to the Mn $2p_{3/2}$ peak position, and the "Off resonance" scan was measured with $h\nu = 639.0$ eV corresponding to an energy off the absorption threshold. From Fig. 5, a large difference between the on and off resonance scans can be seen with an onset at 47.2 eV corresponding to the Mn 3*p* core level. There is another enhanced region from 2.7 to 8.9 eV that can be assigned to the Mn 3*d* and *dp* hybridized states of Mn 3*d* and Sb 5*p*. This assignment arises from comparison to density of states calculations performed on the structural analogs $Ca_{14}MnBi_{11}$ and $Ba_{14}MnBi_{11}$ [10]. This study indicates that the majority *d* states lie in a region centered at 2.7 eV below E_F, and that they hybridize with all states above this region made up mostly of states of *p* character. Accurate identification of the Mn and Sb hybridized states in the valence edge of $Yb_{14}MnSb_{11}$ suffers from the dominance of the Yb^{2+} 4*f* multiplet, but a resonant photoemission scan of the 4*f* region to enhance the Mn states and minimize the Yb states reveals a small contribution of Mn to the valence edge, as shown in Fig. 6.

Fig. 7 shows the wide survey photoemission spectrum of $Yb_{14}ZnSb_{11}$ measured at $h\nu = 1250$ eV. The positions of the core level states for Yb and Sb are present at

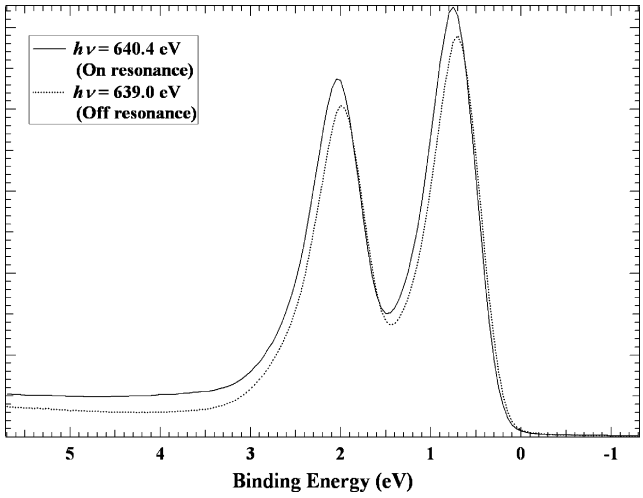

Fig. 6. Resonant photoemission scan of the 4*f* region of $Yb_{14}MnSb_{11}$.

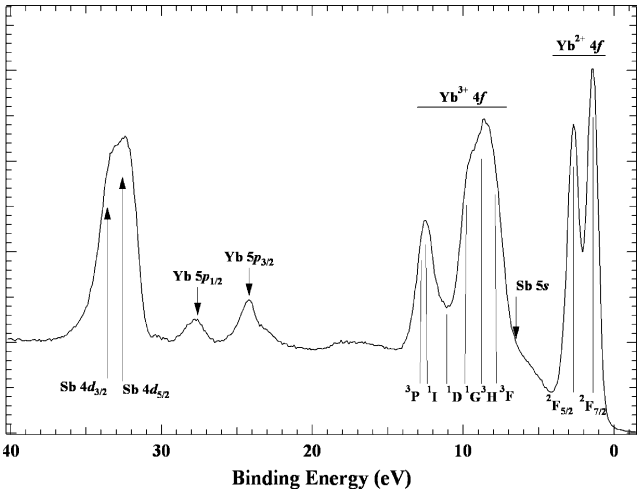

Fig. 8. Valence band scan of $Yb_{14}ZnSb_{11}$ measured at $h\nu = 120$ eV.

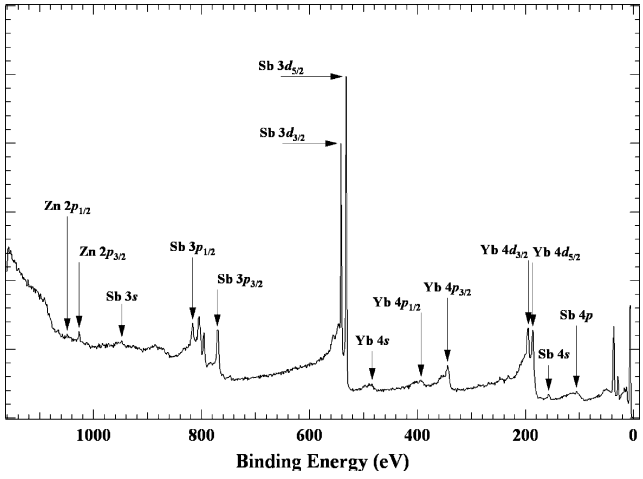

Fig. 7. Wide survey photoemission spectrum of $Yb_{14}ZnSb_{11}$ measured at $h\nu = 1250$ eV.

comparable positions to the Mn analog, and the Zn core levels are also present at their corresponding positions. The Sb 3*s*, $3p_{1/2}$, $3p_{3/2}$, $3d_{3/2}$, $3d_{5/2}$, and 4*s* core levels are observed at binding energies of 948.0, 817.0, 771.0, 542.0, 532.0, and 157.0 eV, respectively, in addition to the Sb 4*p* core level at 106.0 eV. Similarly, the Yb 4*s*, $4p_{1/2}$, $4p_{3/2}$, $4d_{3/2}$, and $4d_{5/2}$ core levels are present at binding energies of 484.0, 394.0, 345.0, 195.0, and 187.0 eV, respectively. In contrast to $Yb_{14}MnSb_{11}$, where the Mn core level *p* states are not well resolved, the Zn spin–orbit split $2p_{1/2}$ and $2p_{3/2}$ core states are clearly observable in the wide survey at 1049.0 and 1027.0 eV, respectively. All of these peak positions correspond within <6 eV of the tabulated peak positions, and the peak separations of the spin–orbit split partners correspond to the tabulated differences to within $\sim$1 eV difference.

Fig. 8 shows the valence band scan of $Yb_{14}ZnSb_{11}$ measured at $h\nu = 120$ eV. In a similar fashion to $Yb_{14}MnSb_{11}$, the general spectral shape of the complete region studied remained consistent over the complete photon energy range studied ($h\nu = 80-200$ eV). The core level, spin–orbit split Sb $4d_{3/2}$ and $4d_{5/2}$ states, and Yb $5p_{1/2}$ and $5p_{3/2}$ states can be seen at 33.60, 32.60, 27.60, and 24.20 eV, respectively. A sharp doublet structure corresponding to the Yb^{2+} 4*f* multiplet is also present at and dominates the Fermi edge region. The final state multiplets of $^2F_{5/2}$ and $^2F_{7/2}$ are slightly broader than the Mn analog and extend over a region of $\sim$4 eV. The broad multiplet structure from the Yb^{3+} 4*d*–4*f* resonance enhanced emission between 4 and 13 eV is also present, but the intensity is much greater than that for the Mn analog and is almost equivalent in magnitude to the Yb^{2+} multiplet. It is clear from a comparison of Figs. 3 and 8 that there is significantly more Yb^{3+} compared with Yb^{2+} or Sb states than that observed in the Mn compound. Fig. 9 shows the analogous fit of the Yb^{3+} region of $Yb_{14}ZnSb_{11}$ using the same energy separations of the final state multiplets of oxidized Yb^{3+}. This figure is qualitatively the same as Fig. 4. However, in this case, the peak that was assigned to Mn 3*d* in Fig. 4 is assigned to the Sb 5*s* states in Fig. 9. The assignment of the Mn state in Fig. 4 was verified with the resonant photoemission experiment shown in Fig. 5. It is possible that the Mn 3*d* orbitals are strongly hybridized with Sb and the peak ascribed to Mn in Fig. 5 is a mix of both Sb and Mn states. In the case of $Yb_{14}ZnSb_{11}$, the small peak in the valence band cannot be assigned to Mn *3d* and is better ascribed to Sb 5*s*. In any case, the presence of Yb^{3+} can be ascribed to both surface oxidation, as seen in the measurements of $Yb_{14}MnSb_{11}$, and to Yb^{3+} intrinsic to the compound because of the significantly larger amount of Yb^{3+}

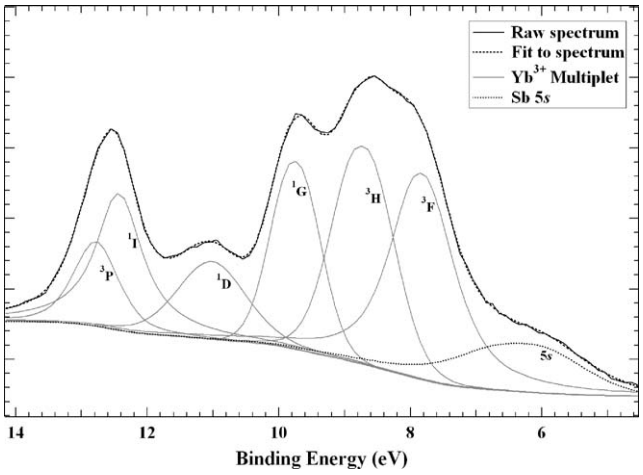

Fig. 9. Gaussian fit of the Yb^{3+} region of $Yb_{14}ZnSb_{11}$ measured at $h\nu = 120$ eV using the same energy separations of the final state multiplets as used for the $Yb_{14}MnSb_{11}$ scan. The background was fit using a Shirley background, and the peaks were fit using seven Gaussian peaks.

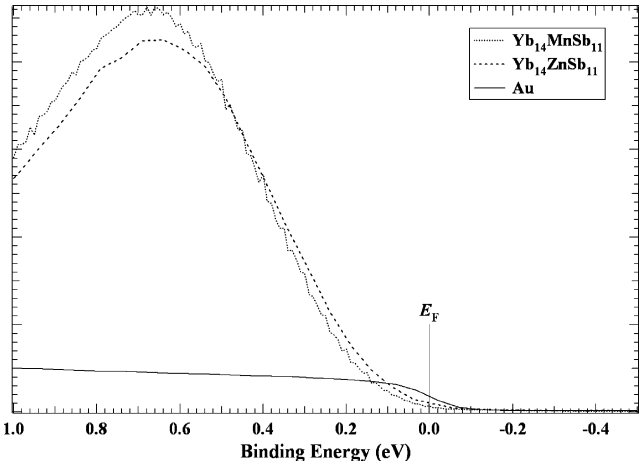

Fig. 10. Comparison of the Fermi edge for $Yb_{14}MnS_{11}$, $Yb_{14}ZnSb_{11}$, and the Au film used to reference E_F.

observed in Fig. 8 compared with Fig. 3. This result is more consistent with the hypothesis of mixed valency for Yb in the Zn analog, supporting the proposal made by Fisher et al. [7].

The intermediate Yb valence was also thought to cause the Fermi energy to cross the Yb 4*f* levels more so than the Mn analog. Fig. 10 shows a comparison of the Fermi edge for $Yb_{14}MnSb_{11}$, $Yb_{14}ZnSb_{11}$, and the Au film used to reference E_F. Both systems have a very low density of states at E_F, and even though both systems are considered metallic conductors (more accurately weakly metallic) [6–7,12], the slow and gradual decrease of the valence edge density of states is more akin to semimetallic behavior as seen in XPS measurements of elemental As, Sb, and Bi [19–21]. $Yb_{14}ZnSb_{11}$ shows a slightly higher Yb 4*f* density of states at E_F indicating slightly more metallic behavior, consistent with experiment, and is in agreement with the proposal of a shift of the Yb 4*f* levels across E_F due to a mixed Yb valency.

In conclusion, the measurements of core and valence electronic states of single crystals of the rare earth transition metal Zintl phases $Yb_{14}MnSb_{11}$ and $Yb_{14}ZnSb_{11}$ are presented in addition to the crystal structure of $Yb_{14}ZnSb_{11}$. The crystal structure is similar to that reported for $Yb_{14}MnSb_{11}$ with the site occupancy factors indicating full occupancies (within the range of their standard deviations) in all sites except a minor deviation for the Zn site. Sample surfaces of $Yb_{14}MnSb_{11}$ and $Yb_{14}ZnSb_{11}$ were measured as received, after Ar^+ ion bombardment, and after cleaving in situ. Detailed analysis of the clean Mn and Zn analog sample surfaces reveal a significant contribution of Yb^{2+} 4*f* states in the valence band region. The samples were found to oxidize even under high vacuum conditions. Analysis of $Yb_{14}MnSb_{11}$ indicates the presence of Yb^{3+} states which are attributed to surface oxidation. Compared to the presence of Yb^{2+} states, the amount of Yb^{3+} is qualitatively considered to be small, consistent with XMCD measurements. The result for the $Yb_{14}ZnSb_{11}$ is consistent with the assignment of an intermediate Yb valence by Zintl counting rules and thermodynamic, and transport studies [7]. Qualitatively, there are significantly larger amounts of Yb^{3+} contributing to the spectrum from a comparison of Yb^{3+} and Yb^{2+} states. While there is some amount of Yb^{3+} that also arises from surface oxidation, the larger amount than that seen for the Mn compound is attributed to the intrinsic presence of Yb^{3+} for $Yb_{14}ZnSb_{11}$. A slightly higher density of states at E_F for $Yb_{14}ZnSb_{11}$ compared to $Yb_{14}MnSb_{11}$ is also observed, and is consistent with the proposal of a shift of the Yb 4*f* states across E_F due to an intermediate Yb valence.

Acknowledgments

We thank R.N. Shelton for use of the magnetometer and P. Klavins for technical assistance. We also thank the staff of the Advanced Light Source and Beamline 4.0 for their assistance. This research is funded by the National Science Foundation DMR-9803074, 0120990, by the Materials Research Institute through LLNL, by Campus Laboratory Collaborations Program of the University of California, and was performed under the auspices of the US Department of Energy by Lawrence Livermore National Laboratory under contract no. W-7405-Eng-48.

References

[1] G. Cordier, H. Schäfer, M.Z. Stelter, Anorg. Allg. Chem. 519 (1984) 183–188.
[2] S.M. Kauzlarich, in: S.M. Kauzlarich (Ed.), Chemistry, Structure, and Bonding of Zintl Phases and Ions, VCH Publishers, Inc., New York, 1996, pp. 245–274.
[3] S.M. Kauzlarich, A.C. Payne, D.J. Webb, in: J.S. Miler, M. Drillon (Eds.), Magnetism: Molecules to Materials III, Wiley-VCH, Weinham, 2002, pp. 37–62.
[4] T.Y. Kuromoto, S.M. Kauzlarich, D.J. Webb, Mol. Cryst. Liq. Cryst. 181 (1989) 349–357.
[5] D.M. Young, C.C. Torardi, M.M. Olmstead, S.M. Kauzlarich, Chem. Mater. 7 (1995) 93–101.
[6] I.R. Fisher, T.A. Wiener, S.L. Bud'ko, P.C. Canfield, J.Y. Chan, S.M. Kauzlarich, Phys. Rev. B 59 (1999) 13829–13834.
[7] I.R. Fisher, S.L. Bud'ko, C. Song, P.C. Canfield, T.C. Ozawa, S.M. Kauzlarich, Phys. Rev. Lett. 85 (2000) 1120–1123.
[8] R.F. Gallup, C.Y. Fong, S.M. Kauzlarich, Inorg. Chem. 31 (1992) 115–118.
[9] A.P. Holm, S.M. Kauzlarich, S.A. Morton, G.D. Waddill, W.E. Pickett, J.G. Tobin, J. Am. Chem. Soc. 124 (2002) 9894–9898.
[10] D. Sánchez-Portal, R.M. Martin, S.M. Kauzlarich, W.E. Pickett, Phys. Rev. B 65 (2002) 144411–144415.
[11] P.C. Canfield, Z. Fisk, Philos. Mag. B 65 (1992) 1117–1123.
[12] J.Y. Chan, M.M. Olmstead, S.M. Kauzlarich, D.J. Webb, Chem. Mater. 10 (1997) 3583–3588.
[13] G.M. Sheldrick, 5.10 Edition, Bruker AXS Inc., Madison, Wisconsin, 1997.
[14] M. Cardona, L. Ley, Top. Appl. Phys. 26 (1978).
[15] S. Suga, S. Ogawa, H. Namatame, M. Taniguchi, A. Kakizaki, T. Ishii, A. Fujimori, S.-J. Oh, H. Kato, T. Miyahara, A. Ochiai, T. Suzuki, T.J. Kasuya, Phys. Soc. Jpn. 58 (1989) 4534–4543.
[16] T. Mori, K. Soda, M. Yamamoto, H. Namatame, A. Ochiai, T. Suzuki, T. Kasuya, S. Suga, J. Phys. Soc. Jpn. 56 (1987) 1465–1469.
[17] L.I. Johansson, J.W. Allen, I. Lindau, M.H. Hecht, S.B.M. Hagström, Phys. Rev. B 21 (1980) 1408–1411.
[18] S.R. Mishra, T.R. Cummins, G.D. Waddill, W.J. Gammon, G. van der Laan, K.W. Goodman, J.G. Tobin, Phys. Rev. Lett. 81 (1998) 1306–1309.
[19] G. Jezequel, Y. Petroff, R. Pinchaux, F. Yndurain, Phys. Rev. B 33 (1986) 4352–4355.
[20] G. Jezequel, J. Thomas, I. Pollini, Phys. Rev. B 56 (1997) 6620–6626.
[21] H. Tokailin, T. Takahashi, T. Sagawa, K. Shindo, Phys. Rev. B 30 (1984) 1765–1772.